Journal of Computers Vol. 35 No. 4, August 2024, pp. 11-30
doi: 10.53106/199115992024083504002

An Attuned Data Extraction Model for Maximizing Ocean Surface Wind Prediction Using Scatterometry

Yuge Liu, Ying Huang*, and Zhiyou Yang

Liuzhou Railway Vocational Technical College,
Liuzhou Guangxi, China
rico-penny@ltzy.edu.cn, huangying800816@163.com

Received 3 April 2023; Revised 3 April 2023; Accepted 19 April 2023

Abstract. Scatterometers equipped with C-bands are deployed along the coast surface for measuring ocean and sea surface winds and roughness. Deployed in low orbital satellites, the electromagnetic signals transmitted are scattered at the ocean's surface from which the intensity and wind direction are detected. Wind intensity is impacted by different features such as salinity, scattering index, obstacles, etc., resulting in erroneous predictions. This article introduces an Attuned Data Extraction Method (ADEM) for detecting precise wind intensity and direction. The fore-mentioned errors are addressed using multimodal data fusion to prevent the density seizure problem. This density seizure is caused due to inappropriate/ irrelevant sensing. The above classification uses a random forest learning paradigm for each sensing instance. The classification refers to the inappropriate and irrelevant data observed during speed estimation. The classification is necessary to balance the variations in wind speed and intensity observed from different points. The unclassified data is neglected from the fusion process, preventing errors in the forecast. Besides, the fusion is performed in two distinct levels: extracted and attuned. In the extracted fusion data, the classified data is exploited without alignment; the attuned fusion requires error correction to improve the precision. The joint fusion data scales are utilized for improving the sensing device data consistency with less computing time and errors.

Keywords: data fusion, ocean monitoring, random forest, scatterometer, wind prediction

1 Introduction

Wind speed estimation is major in weather detection, cyclone attack prediction, and global navigation satellite system (GNSS). Wind speeds are estimated or measured by an anemometer which helps to produce an accurate speed rate of wind [1]. On the other hand, an anemometer increases the complexity, maintenance, and cost of the system, reducing the reliability and efficiency of the system. To overcome these problems, machine learning (ML) algorithms are mostly used in wind speed estimation [2]. ML, like long short-term memory (LSTM) and Convolutional neural network (CNN), helps to increase the accuracy ratio in the estimation progression [3]. Synthetic aperture radar (SAR) is a system used in wind speed prediction and estimation processes that produces a proper dataset for the estimation procedure. SAR decreases the error and failure rate in the estimation process by providing accurate data about current and previously recorded wind data [4]. The Bayesian inversion method is used in wind speed estimation by calculating both the dropper and black shift scatter produced by SAR. Black shift scatter is estimated using scatter plots of different wind in decreasing order. Any change in the order results in varying phenomena of the speed estimation. The bayesian method improves the accuracy ratio and efficiency rate in the wind speed estimation procedure by when compared with other methods. The Timeshift strategy is also used in the wind speed estimation process with the help of the Compressive sensing (CS) method, which evaluates the data based on certain conditions and features [5-6].

Wind speed estimation is also done based on the data extraction process, which mostly analyzes the information stored in the data or produced by SAR. The data extraction process extracts the exact features from the database, which is done based on certain features [7]. Comparing current and previously recorded video produces a proper data set for the extraction process. Extreme learning machine (ELM) is one of the data extraction processes used to estimate wind speed rate based on wind turbine parameters [8]. ELM also estimates sensorless information collected by SAR, increasing the system's overall efficiency. The global digital elevation model (GDEM) is based on an extraction process that extracts wind turbine parameters data [9]. Improved extreme wind speed

* Corresponding Author

estimation plays a vital role in the estimation process, which analyzes details such as characteristics, features, location, and direction [10]. Data extraction is also done using the Global navigation satellite system (GNSS). Dropper maps are used here to locate the direction and location of certain places and extract accurate data for the estimation process. Dropper maps provide exact information from satellite and radar observation. GNSS is cost-effective and reduces energy and time consumption rates, which aids in increasing the system's total performance [11].

Synthetic aperture radar (SAR) is a critical remote sensing technology that captures accurate information and data about wind. SAR plays a vital role in the wind speed estimation, prediction, and detection process, which helps to increase the safety of people by increasing the accuracy ratio in the estimation progression [12]. Most of the estimation process is based on SAR and the Digital elevation model (DEM). A data fusion-based wind estimation method increases the overall accuracy rate in calculating wind speed prediction [13]. Interferometry SAR (InSAR) sensors improve the system's overall performance by providing an accurate wind speed rate. InSAR is a three-step sensing approach that analyzes every detail of data to get an accurate speed rate of wind [14]. InSAR also finds out the wind speed with unproper data recorded by SAR. A machine learning (ML) algorithm named artificial neural network (ANN) is also used in data fusion-based wind estimation. ANN has been done based on the extraction process, which is done based on certain features such as weather conditions, wind direction, location, etc. The ANN-based approach increases the accuracy ratio in wind speed estimation progression and increases the system's overall performance [15-16]. The existing systems utilize the ocean surface's electromagnetic signals to identify the wind direction. However, the wind intensity has been influenced by different factors, such as scattering index, salinity, and obstacles, which affect the wind direction detection efficiency. Applying the Attuned Data Extraction Method (ADEM), this research issue is overcome. The ADEM method uses the multi-model data fusion process that helps predict wind intensity and direction. Multimodal data fusion predicts and classifies wind speed and intensity. The wind intensity is impacted by various features such as scattering index, salinity, obstacles, etc., resulting in erroneous predictions. The errors are addressed using multimodal data fusion to avert the density seizure issue. This density seizure is caused because of irrelevant/inappropriate sensing. The classification utilizes a random forest learning model for every sensing instance. The classification defines the wrong and inappropriate data observed during speed estimation. The classification is essential to balance the variations in wind speed and intensity observed from dissimilar points. The unclassified data is ignored from the fusion progression, preventing errors in the forecast. The successive use of the data fusion model decreases the density seizure issue. Then the created system's efficiency is assessed utilizing experimental outcomes. This article proposes the following contributions:

i. Designing an attuned data extraction method for processing and detecting precise wind speed from the variational data.
ii. Incorporating a classification learning process for distinguishing irrelevant and inappropriate data from different observation sequences.
iii. Performing a precise data extraction from the fusion process to prevent detection error.

2 Related Work

Chen et al. (2020) proposed an adaptive wind retrieval algorithm based on the information entropy method for GaoFen-S synthetic aperture radar (SAR). Images are identified reliant on the maximum information entropy method used here to analyze the images stored in the database. The proposed method finds field retrieval algorithms that extract the exact details about the SAR images available on the database. Numerical outcomes demonstrate that the suggested method improves the effectiveness of retrieving wind information from SAR images [17]. However, this model has limitations, which are primarily reproduced in its incapability to automatically recognize the absence or presence of wind streaks in SAR imageries, and in the computation of wind speed, the incapacity to tune a more appropriate GMF for GF-3 because of the absence of adequate GF-3 SAR imageries.

Li et al. (2019) proposed an impact of sea state on wind retrieval based on sentinel-one wave mode data. Synthetic aperture radar (SAR) finds the images calculated based on stored data. The proposed method determines the accurate wind speed calculated by buoys. Furthermore, sea state impacts are identified based on the Scatterometer analysis process. Compared with other methods, the suggested model enhances the accuracy ratio in identifying wind speed and the impact of sea state [18]. However, this study is not addressed the impact of the operational wind retrieval point of view.

Chu et al. (2020) introduced a heterogeneous multi-model deep learning method (HMDL) for wind speed retrieval. Global navigation satellite system space reflectometry (GNSS-R) is used here to find accurate information for ocean wind speed retrieval systems. In addition, satellite receiver state (SRS) parameters play a vital role in HMDL, which enhances the system's efficiency and effectiveness. Experimental result shows that the recommended HMDL technique improves the accuracy ratio in the prediction [19]. However, the accuracy of the wind speeds regimes with a small number of samples.

Wan et al. (2021) proposed a new compressive sensing (CS) method using a timeshift strategy for the wind speed prediction process. The random sampling method is used to evaluate the given data set by comparing it with previously recorded data, which helps get accurate information for the prediction process. Compared with other traditional techniques, the suggested CS method enhances the overall performance and effectiveness of the system by improving the accuracy rate in the wind speed prediction progression [20]. However, wind speed signals from the random sample cannot be deprived of that, such as other compressive sensing approaches; the suggested method is lossy compressions.

Geng et al. (2021) introduced a Spatiotemporal correlation graph neural network for wind speed forecasting systems. The LSTM approach finds the temporal correlation in high-dimensional spatial features. Furthermore, the graph optimization method is used here to analyze the multiple nodes available in the database and produce proper data set for prediction. Numerical outcomes demonstrate that the suggested technique performs better than conventional approaches by increasing the system's accuracy rate [21]. However, temporal pattern attention cannot extract every data conducive to the prediction from many time stages when the span predictive time horizon was large.

Elyouncha et al. (2021) introduced the joint retrieval method of ocean surface wind and current vector using the Bayesian inversion method from synthetic aperture radar (SAR). Both doppler frequency shift and black scatter are measured or calculated by the SAR system, which has a huge amount of data for analysis. Compared with other approaches, the recommended technique finds out the actual wind and surface rate of the ocean, which aids to improve the system's overall performance [22]. However, the poor temporal resolution of SAR limits its ability to track fast-evolving atmospheric characteristics.

Prajapati et al. (2022) proposed an assessment of synthetic aperture radar (SAR) by using the numerical model for the wind speed prediction process. First, the global forest system (GFS) is used to find the wind speed by calculating the information produced by SAR. Then, wind speed is calculated by buoys by observing the information given by GFS. Compared with other methods, the proposed numerical model increases the accuracy in validating wind speed [23]. However, the wind speed differences are large concerning previous studies with Buoy (1.02 m/s), and ASCAT (1.78 m/s) because model winds have limitations.

Zhu et al. (2020) introduced a semi-empirical algorithm based on Gaofen-3 (GF-3) for wind speed retrieval. Synthetic aperture radar (SAR) provides appropriate information about previously recorded wind speed. The proposed method calculates both the vertical and horizontal velocity of the wind, which helps to find out the accurate speed of the wind. Geophysical model fiction (GMF) is used here to calculate wind speed retrieval from SAR [24]. The author only illustrates the denoised outcomes utilizing an empirical technique based on the limited data collection.

Ferrer-Cid et al. (2020) proposed a multi-sensor data fusion calibration method for the Internet of Things (IoT) air pollution platform. The calibration process combines linear and non-linear information produced by the sensor. In addition, machine learning algorithms are also used here to improve the system's efficiency. The experimental result shows that the recommended technique increases the calibration process's accuracy ratio [25]. However, if the different sensors utilized in fusion were extremely correlated, the multi-collinearity phenomenon may appear, which causes difficulties in the learning algorithm.

Yu et al. (2021) proposed a multisystem interferometric data fusion framework for wind speed prediction. Synthetic aperture radar (SAR) sensors capture every detail about wind and produce a proper dataset for the analysis process. The suggested technique uses the phase unwrapping and phase fusing process to get accurate details about wind, which plays a vital role in prediction. Furthermore, the recommended technique increases the efficacy and effectiveness of the system [26]. However, if the phase unwrapping result is incorrect, an additional non-zero integer can be auxiliary to the ideal ambiguity numbers of the unwrapped stage, whose numerical mean cannot be measured as 0 (unlike the phase noise).

Snauffer et al. (2018) introduced a data fusion method for environmental process control using ML algorithms. Artificial neural network (ANN) and Random forest (RF) approaches are used here to evaluate the data stored in the database based on certain features. Simulation outcomes illustrate that the recommended method improves the system's accuracy, efficiency, and speed, which aids in increasing the network's total performance [27]. Therefore, the findings in this study were relevant to the task at hand and to other complex small data problems

for which computational cost is low and the cost of gathering training data is comparatively high.

Nilsen et al. (2019) introduced a novel synthetic aperture radar (SAR) ocean wind retrieval approach. The proposed method is based on parameters named azimuth phase, integral cross spectra, and range phase, which are calculated based on images captured by SAR. Compared with other methods, the proposed approach provides better service and performance by increasing the accuracy rare in calculating wind speed [28]. However, the sparse recovery must be performed for each local image, thus increasing the total computational cost.

Shao et al. (2021) proposed a new evaluation process for sea surface wind and waves based on HY-2B data. Significant wave height (SWH) is calculated based on the velocity and height of waves on the sea and provides proper data for the evaluation process. Compared with other methods, the suggested technique improves the efficiency and effectiveness of the system by increasing the accuracy ratio in the wind speed prediction progression [29]. However, the error became scattered at significant wave heights larger than 10 m due to inadequate samples.

Giangregorio et al. (2018) introduced an ocean wind speed estimation process based on the Global navigation satellite system (GNSS). Dropper maps play a vital role in the proposed method, which helps to calculate the accurate location and place. Furthermore, the least-squares matching method is used here to compare the information provided by GNSS with previously recorded data. Numerical outcomes demonstrate that the suggested technique increases the overall accuracy ratio in wind speed estimation [30]. However, the accuracy of the retrieved wind speed was affected mainly by the correctness and applicability of simulated models and the calibration of the satellite acquisition.

3 Attuned Data Extraction Method (ADEM)

The proposed ADEM model is introduced to improve the sensing device data consistency of the C-band scatterometer for measuring sea and ocean surface winds and roughness. The forecast of heavy wind or roughness in the ocean's surface through the forecast center in definite sensed data on better accuracy for its function. The transmitting electromagnetic signals are scattered or diffused from the deployed low orbital satellites based on the intensity detection and wind direction detection of the ocean's surface. Some common features, such as salinity, obstacles, scattering index, etc., are prominent factors resulting in erroneous predictions through data fusion. ADEM is a data extraction method that uses random forest learning to classify seizure data and accumulated data. The attuned method means fusing the data from various resources and performing the wind detection process to improve overall system performance. In Fig. 1, the proposed method's process is illustrated.

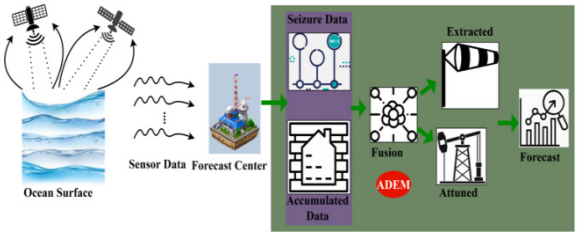

Fig. 1. Proposed method's illustration

The function of ADEM in electromagnetic signals based ocean's surface intensity and wind direction detection acquires precise wind intensities and its directions prediction through a scatterometer sensor placed in the satellite. The wind predictions are classified using random forest learning using the seizure and accumulated data. The classification result is aided in detecting the intensity and wind direction through data fusion from the already stored data. The function of ADEM is represented in Fig. 1 where the sensed data was initially analyzed. The input electromagnetic signals-based sensor data is represented as

$$C_d^s = \frac{1}{d}\left\| \sum_{i=1}^{d} I_x(O_{in}) \cup D_y(O_{in}) \right\|. \quad (1)$$

Such that,

$$\left.\begin{aligned} I_x(O_{in}) &= \frac{1}{d}\int_{-\infty}^{\infty} \frac{\frac{x_i(O_{in})}{O_{in}} dO_{in}}{x_i(O_{in})} \\ &\quad and \\ D_y(O_{in}) &= \frac{1}{d}\int_{-\infty}^{\infty} \frac{y_i(O_{in})}{O_{in}} dO_{in} \end{aligned}\right\} \quad (2)$$

As per the above equations (1) and (2), the variables $I_x(O_{in})$ and $D_y(O_{in})$ represented the wind intensity and direction of the sensed data. According to the observation intervals C_d^s concerning measuring ocean and sea surface winds and roughness in the x and y-axis. The variable D represents the wind direction, and I represents wind intensity. The process of attuning improves data assimilation and availability. Based on the observed data at different intervals, attuning takes place. This attuning is required for extracting precise data. This differs from the conventional method by assimilating similar featured data based on observations. The seizures are identified from fusion and missing data such that the variations in errors and estimations are mitigated. The intensity and direction help to identify the intervals to be taken for measuring the wind speed. The fusion is executed in two distinct levels: attuned and extracted. In the extracted fusion information, the classified data is employed without alignments; the attuned fusion needs error correction to enhance accuracy. The attuned process denotes fusing the information from different resources and executing the wind detection progression to enhance total system performance. Similarly, d measures sea or ocean surface winds and roughness detection. If x and y planes increase and decrease concerning different observation intervals O_{in}, then $x \in [0, \infty]$ and $y \in [-\infty, 0]$ and therefore,

$$\left.\begin{aligned} I_x(O_{in}) &= \frac{1}{d}\int_{-\infty}^{\infty} \frac{x_i(O_{in})}{O_{in}} dO_{in} \\ D_y(O_{in}) &= \frac{1}{d}\int_{-\infty}^{\infty} \frac{y_i(O_{in})}{O_{in}} dO_{in} \end{aligned}\right\} \quad (3)$$

Based on the above equation (3), the initial wind intensity and direction are detected by the scatterometer for all $I_x(O_{in}) + D_y(O_{in})$ that represents a complete consequence based on x and y nodes for an observation time interval on $(F \times T)$. Here, F is the forecast center process. The forecast center is performed to broadcast the changes in wind direction present in C_d^s. Changes in wind direction due to the electromagnetic signals transmitted in the functioning system while acquiring C_d^s in any T. This sequence of instances follows a high-sensing device data consistency process that is illustrated as follows in equation (4).

$$\left.\begin{aligned} I_x(T) &= \frac{x_i(O_{in})}{T} * 2^{\frac{e}{2}} N_i[F \times T - 2^e] \\ &\quad and \\ D_y(T) &= \frac{y_i(O_{in})}{T} * 2^{\frac{e}{2}} N_j[F \times T - 2^e] \end{aligned}\right\} \quad (4)$$

Where,

$$\left.\begin{array}{c} N_i = E^s(T)\left|\frac{e}{2}\right| E^s(T)_{e-1} \\ and \\ N_j = E^s(T)^{-1}\left|\frac{e}{2}\right| E^s(T)_{e-1} \end{array}\right\} \quad (5)$$

Where the factors N_i and N_j are the nodes-transform transmitters for high and low wind changing rates. Similarly, the variables $E^s(T)$ and $E^s(T)^{-1}$ represents the direct transform and inverse transform of electromagnetic signals N_i and N_j transmitted are scattered (diffused) at the sea surface. The direct or indirect transmitting signals are used based on the occurrence of the partial nodes (i.e.) the x or y plane. The variable represents the erroneous predictions of the wind intensity in both the process of node identification. Now, the wind data intensity node based C_d^s is determined as in equation (5).

$$\left.\begin{array}{c} C_d^s[E^s(T)] = \frac{2^{\frac{e}{2}}[(F\times T)-2^e}{T^2}[C_i - C_j] \\ and \\ C_d^s[E^s(T)] = \frac{2^{\frac{e}{2}}}{T}[\int_0^{\infty}\frac{C_i[(F\times T)-2^e]}{T}dT - \int_{-\infty}^{0}\frac{C_j[(F\times T)-2^e]}{T}dT \end{array}\right\} \quad (6)$$

From the above equation (6), is the wind data intensity of fore-mentioned errors-less $C_d^s[E^s(T)]$ that is identified after performing multimodal data fusion. Based on this $C_d^s[E^s(T)]$, the sensed data can be classified into two, namely seizure data and accumulated data are processed for further classification. The above equation (6) is aided in estimating the seizure data (Sz_D) and accumulated data (A_D)

$$\left.\begin{array}{c} Sz_D = \frac{1}{2\pi(F\times T)}\left|\sum_{d=1}^{T}(x_d - y_d)E^{s-\sigma}\right|, \forall j = i+1, i \in e \\ and \\ A_D = -\sum_{i=\delta_e}^{\delta_d} Sz_D \log Sz_{D_i} \end{array}\right\} \quad (7)$$

In equation (7), the variable σ denotes the point on the normal x and y plane, δ_d and δ_e are the high and low wind intensity and density of Sz_D observed. Fig. 2 illustrates the fusion process for seizure and accumulated data in different intervals.

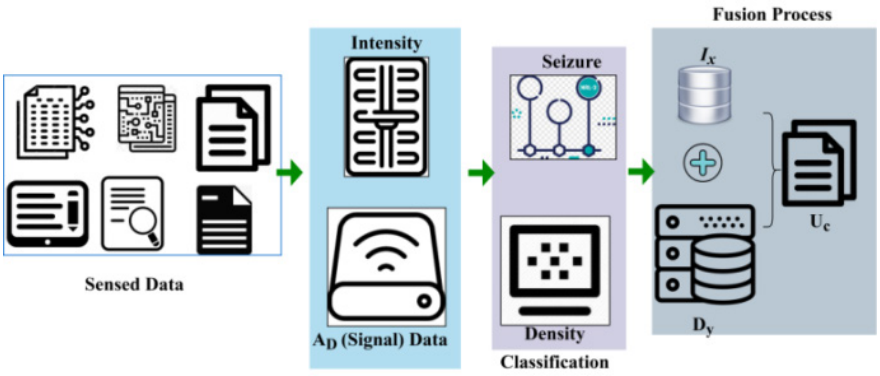

Fig. 2. Fusion process illustration

The fusion process distinguishes $I_x(O_{in})$ and A_D based on N_i and N_j. This is required for e detection from $SZ_D \forall A_D$ and hence the $I_x(T)$ and $D_y(T)$ are assimilated. Post the classification process, fusion $\forall I_x \in A_D$ and $D_y \in (N_i \oplus N_j)$ is performed to obtain U_C. This U_C is valid for attuned extraction with fewer errors (Fig. 2). The wind data intensity of Sz_D generates the A_D for the $E^s(T)$ as in equation (8)

$$A_D[E^s(T)] = \frac{A_D}{\log\left[\frac{T}{\delta_d - \delta_e}\right]} \tag{8}$$

Similarly, the errors mentioned above are noticed using multimodal data fusion process to detect the density seizure problem. The inappropriate or irrelevant sensing data observation caused density seizure (D_{Sz}) is computed as in equation (9)

$$\left.\begin{aligned} D_{Sz}\left[A_D, T, E^s(T)\right] &= -\sum_{i=1}^{F} T_i - \sum_{j=1}^{O} T_i - \sum_{i=1}^{O}\sum_{j=1}^{O} T_i\sigma_i \\ &\quad instead \\ D_{Sz}\left(A_D\left[E^s(T)\right]\right), Sz_D &= \begin{cases} -\sum_{i=1}^{O} T_i\sigma_i \frac{1}{c_i}, if\ x_d(T) \in [0,\infty] \\ -\sum_{i=1}^{O} T_i\sigma_i c_j, if\ x_d(T) \notin [0,\infty] \end{cases} \end{aligned}\right\} \tag{9}$$

This density seizure problem is prevented by a multimodal data fusion process for transmitting signals $A_D[E^s(T)]$ and Sz_D alone with the different observation instances and intervals. Based on this classification helps to address the inappropriate sensing detected by the scatterometer and wind prediction for all $I_x(T)$ or $D_y(T)$ or both nodes. The classification process is based on Sz_D and $A_D[E^s(T)]$ using random forest learning. The classification process is illustrated in Fig. 3.

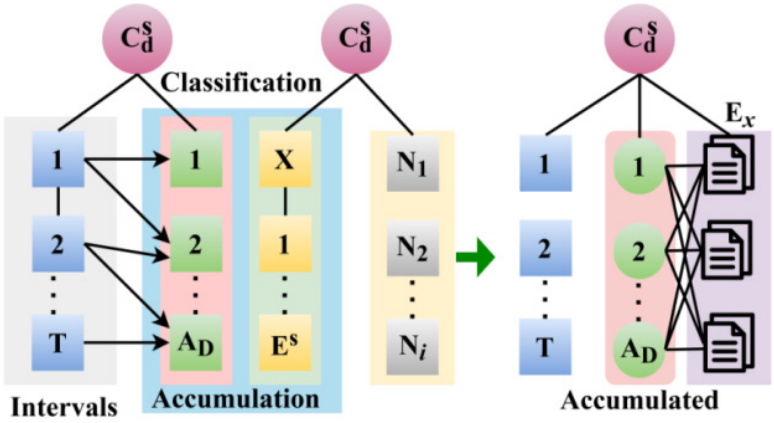

Fig. 3. Classification process

The classification process is performed for A_D and $N_i \forall T$ such that A_D from T generates E_x. Based on the mapping between T's sequence in A_D, the E^S is segregated. This is mitigated in E_x by validating N_i and N_j as in equation (5). The error data accumulated in E^s is separated for further analysis from $E_x \in U_C$ ($A_D[E^s(T)]$) other than $U_C[Sz_D, T]$ (Refer to Fig. 3). In this classification process, the above features are identified and analyzed at each level, followed by sensing instances. The input and unclassified data are defined in equations (10) and (11) for the Sz_D and $A_D[E^s(T)]$.

$$U_C[Sz_D, T] = \frac{e^{-D_{Sz}[A_D, T, E^S(T)]}}{\sum_{i=1}^{F\times T} e^{-D_{Sz}[A_D, T, E^S(T)]_i}}. \quad (10)$$

In equation (10), $D_{Sz}[.]$ represents the random forest function for Sz_D and $U_C[.]$ is the initial sensing sequence at T. Similarly, the initial sensing sequence of the fusion process and forecast errors are given for $A_D[E^s(T)]$ as

$$U_C(A_D[E^s(T)]) = \frac{e^{-D_{Sz}[A_D, T, E^S(T)]}}{\sum_{i=1}^{T} e^{-D_{Sz}[A_D, T, E^S(T)]_i}}. \quad (11)$$

As per equation (11), the extracted and attuned fusion of the machine learning is represented such that $D_{Sz}[A_D, T, E^s(T)]$ is estimated for both the nodes $\in C_d^s[E^s(T)]$. This assists in distinguishing the transmitting signals based on T to facilitate classification sequences. The extracted fusion of the forest learning process reliant on $C_d^s[E^s(T) \in [-\infty, \infty]]$ and $x_d \in [0, \infty]$ or $y_d \in [-\infty, 0]$. The condition of $x_d \notin [0, \infty]$ fulfills a precision of $[-\infty, 0]$ that indirectly illustrates y_d at different observation interval instances T. The precision of $C_d^s[E^s(T)]$ is independently using $U_C[.]$ where in the neglected fusion process $U_C[.]^*$ represents that the precision of $x_d \notin [0, \infty]$ is exploited, and therefore, the previous observation $U_C[.]$ does not hold for further identifications. As per the above, $x_d \notin [0, \infty]$ is considered. These error corrections (EC) are approximated with the extracted to attune fusion of the final result (M). Therefore, the extracted fusion solution instance (i.e.) $\{E_{x(F\times T)}\}$ for both, the fusion inputs are estimated for their precision in equations (12) and (13).

$$E_{x(F\times T)} = C_d^s[E^s(F\times T)] - \frac{\delta_{F\times(T-1)}}{D_{Sz}[A_D, T, E^s(T)]_{F\times(T-1)}}, \forall C_d^s = I_x(O_{in}) + D_y(O_{in}). \quad (12)$$

Contrarily,

$$E_{x(F\times T)} = C_d^s[E^s(F\times T)] - \delta_{F\times(T-1)} \times D_{Sz}\left[A_D, T, E^s(T)\right]_{F\times(T-1)}, \forall C_d^s = I_x(O_{in}) + D_y(O_{in}). \quad (13)$$

The above equation δ is the fusion point at which $C_d^s[E^s(T)]$ is distinguished from $C_d^s = I_x(O_{in}) + D_y(O_{in})$ to $I_x(T)$ or $D_y(T)$ alone. If it forecasts the fusion data of separation and then observation time is the considerable metric (i.e.) addressing $C_d^s[E^s(T)]$ as the operation of T to identify reliable observation. This is because the sensed data variation follows various observation interval sequences based on wind prediction analysis and neural stimuli. Here, the fusion data output for $C_d^s[E^s(T)] \neq I_x(T)$ is given as in equation (14).

$$E_{x(F\times T)} = C_d^s[E^s(F\times T)] - \delta_{F\times(T-1)} \times \frac{1}{T}\left\{\begin{matrix} D_{Sz}\left[A_D, T, E^s(T)\right]_{F\times T} - \\ D_{Sz}[A_D[E^s(F\times(T-1)), Sz_D]_{F\times(T-1)} \end{matrix}\right\}. \quad (14)$$

The fusion on the (x, y) axis represents the differing signals C such that $E_{x(F\times T)} \notin I_x$ or $E_{x(F\times T)} \in I_x \leq C \leq E_{x(F\times T)} \in (I_x + D_y)$ is the precise output for classifying $C_d^s[E^s(T)]$. If the conditions mentioned above are not satisfied, then the erroneous predictions increase by one. In other words, if the condition $E_{x(F\times T)} \in I_x$ is observed, and then $EC = EC + 1$ else sensing device data consistency $SD = SD + 1$. Improving the SD other than the appropriate EC and features is prominent in the classification process. From this assessment, both independent and joint fusions are induced for all the extracted fusion output as in equations (12), (13), and (14). The extraction process is illustrated in Fig. 4.

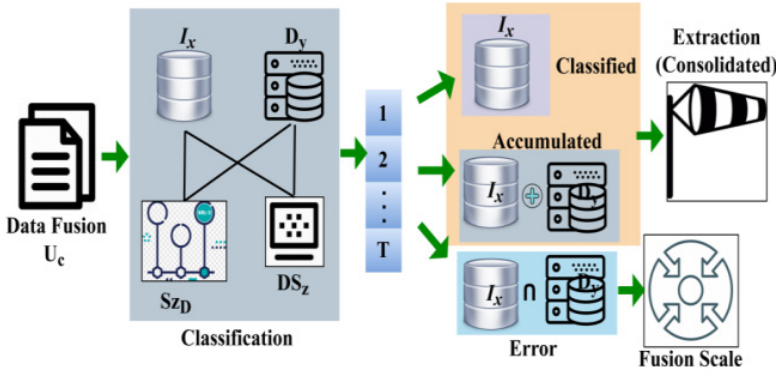

Fig. 4. Data extraction process

The fused data U_c without E^s is classified further for I_x, D_y, SZ_D, and DS_z instances. Based on I_x and D_y classified I_x (or) accumulated C_d^s (i.e.) $[I_x \oplus D_y]$ is exploited. Contrarily, if $I_x \cap D_y$ is observed, then fusion scale analysis is performed. In the extracted data $\frac{MT}{dT}$ is performed (i.e.) consolidated extraction (Fig. 4) is performed. In the extraction process, DS_z and SZ_D are reduced (Diminished) to prevent errors. The deviation between the transmitting signals equation assists in approximating the sequence of EC and SD, which helps to increase the fusion of classification. In evaluating attuned fusion outputs, the result is discontinuous based on the occurrence of C. Hence, the output does not utilize the same processes for all $T = \{1, \text{to } T \times F\}$. If a joint fusion scale occurs, then $EC = EC + 1$, and this estimation is consolidated concerning T as in equation (15)

$$\frac{MT}{dT} = \left(\frac{E_x T}{dT} + \frac{(1-\delta) A_x T}{dT} \right) - \delta \frac{A_y T}{dT}. \tag{15}$$

Where,

$$\left.\begin{aligned} E_x = E_{x(F\times T)} \in \{ I_x(O_{in}) + D_y(O_{in}) \} \\ A_x = E_{x(F\times T)} \in I_x \\ A_y = E_{x(F\times T)} \notin D_y \end{aligned}\right\} \tag{16}$$

In equation (16), the solution is not the final as the last attuning data is based on $\frac{MT}{dT}$ using the joint fusion scales computation. Similarly, changes in predictions vary the fusion of EC and SD by approximating δ with the E_x depends upon the solution of $\frac{MT}{dT}$ transmitting signals. The precision of $E_x + (1-\delta)\, A_x$ features at some T wherein either E_x or A_x is augmented. In particular, the sequence with high EC is increased for the transmitter. The following consequence of equations represents the joint fusion scale for deriving M based on the extracted data fusion solution as in equations mentioned above, respectively.

$$\left.\begin{aligned} M = \int_{-\infty}^{\infty} \left(C_d^s \left[E^s \left(F \times T \right) \right] - \frac{1}{D_{Sz} \left[A_D, T, E^s(T) \right]_{F\times T-1}} \right) \frac{t}{dt}, \ if \ \delta_{E^s} = 1 \forall T = 1 \ to \ F \times T \\ and \\ M = \int_{-\infty}^{\infty} C_d^s \left[E^s \left(F \times T \right) \right] \frac{T}{dT}, \forall D_{Sz}[.] = 1 \ (i.e.) E_x[E^s(T)] = I_x(O_{in}) + D_y(O_{in}) \end{aligned}\right\} \tag{17}$$

In equation (17), is the series solution of the transmitting signal forecasts processing. From $\delta = D_{Sz}[.] = 1$ the result must not exploit any features or EC consistency. Now, attuned fusion is performed based on obtaining data. Similarly, the transmitting signals approximation of E_x, A_y and M as per δ is illustrated, respectively. The device data consistency solution of M for all $E_{x(F\times T)} \notin I_x$ or $E_{x(F\times T)} \in I_x \leq C \leq E_{x(F\times T)} \in (I_x + D_y)$. It represents that $C_d^s[E^s(F \times T)]$ is an operation of T in the different wind observation time intervals instances are responsible for improving the assessment.

Instead, the joint fusion scale approximation of M based on δ, the entire metric is $C_d^s[E^s(T)]$ is the estimation factor. If $E_{x(F\times T)} \in I_x \not< E_{x(F\times T)} \in (I_x + D_y)$, the erroneous predictions are increased that is suppressed for its estimation using $E_x[E^s(T)]$. The fusion process is frequently utilized depending on the accumulated and extracted data of M using the condition $E_{x(F\times T)} \in I_x$ and $E_{x(F\times T)} \in (I_x + D_y)$. The D_{Sz} $[A_D, T, E^s(T)]_{F\times T}$ conditions are identified as remaining observations at the interval of attuned data extraction, and therefore, the sensed data are not prolonged for detection. The further observations are forecasts between the appropriate sensing instances based on dT. The forecast wind prediction is also maximized for the remaining observations without increasing the computing time and errors of the ocean and sea surface winds and roughness detection. The remaining sensed device data increases computation time and increases erroneous predictions. This changes the data fusion as in equation (7), and hence $[A_D, T, E^s(T)]$ is used for assigning the precision to the remaining observations, thereby reducing the number of errors. The ocean monitoring and analysis follows both independent and joint precision for $I_x(O_{in})$ and $D_y(O_{in})$ and therefore, the forecast rate is high. Table 1 presents the seizure and e estimation for different observed wind speeds.

Table 1. Seizure and e for different wind speeds

Observed wind speed (m/s)	A_D/ Interval	e	Sz_D
1.2	21	+0.1	2
3.8	3	-0.13	0
4.2	16	-0.102	3
5.4	25	+0.12	7
6.3	12	-0.1	2
7.8	32	+0.25	8
9.6	41	+0.28	10
10.5	48	+0.32	9
11.7	51	+0.34	11

In Table 1, the e and Sz_D for different observed wind speeds is presented. The e and SZ_D identification is performed for I_x and D_y such that U_C generates errorless data. Depending on the E^s classification, the e factor is identified from U_C (A_D $[E^S(T)]$). Contrarily, the seizure data depends on $E_{x(F\times T)}$ from C_d^s analyzed in different $U_C \in T$. Therefore, Sz_D is less if the density is less, contrarily, e is high. This is rectified in the consecutive observations $T \forall E^S$ and A_D. Fig. 5 and Fig. 6 illustrate the observed speed and its corresponding precision and error factor.

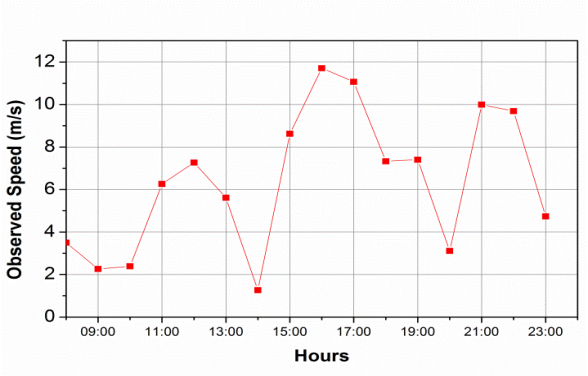

Fig. 5. Observed wind speed

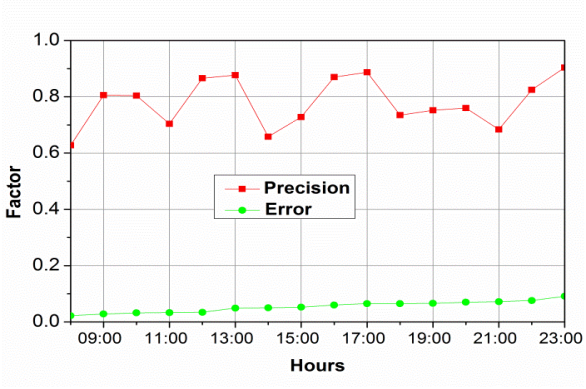

Fig. 6. Precision and error

Fig. 5 presents the observed wind speed and corresponding precision and error factors for different periods. The precision is improved by performing fusion mitigating SZ_D and e from different T such that N_i and N_j are used for addressing the error based on issues. In the classification process, further assessments are performed by preventing E^s interruption in U_C. Therefore for any E^s occurrence in T, the classification is performed for A_D and N_j without N_i in maximizing precision. Therefore, $\frac{MT}{dT}$ is exploited for maximizing precision wherein the error is confined. For different hours, the SZ_D estimated from the observed data is illustrated in Fig. 6. The SZ_D is computed for $e \in E^s$ and $D_y(T)$ experienced in A_D. For distinguishable $E_{x(P\times T)}$, the $\frac{MT}{dT}$ generates DS_z and hence the non-intensity and e data are disconnected. This further interrupts e in the wind prediction process, maximizing the analysis. Table 2 presents the error, predicted wind speed and direction for different hours, and its corresponding stats. The stats provide data for minimum, maximum, and average wind speeds observed in a particular hour.

Table 2. Error and Predicted wind speed and direction for different hours

Hour	Stats	Wind speed (m/s)	Direction (deg)	Error
8:00	Minimum	1.2	51.3	0.041
	Maximum	7.6		0.087
	Avgerage	4.4		0.064
12:00	Minimum	3.2	209.6	0.022
	Maximum	10.6		0.071
	Avgerage	6.9		0.0465
16:00	Minimum	2.8	185.8	0.034
	Maximum	8.5		0.084
	Avgerage	5.65		0.059
20:00	Minimum	5.1	298.6	0.048
	Maximum	11.7		0.089
	Avgerage	8.4		0.0685
24:00	Minimum	4.6	241.58	0.052
	Maximum	10.9		0.091
	Avgerage	7.75		0.0715

In Table 2, the wind speed, direction, and error observed in different time hours is presented. The minimum, maximum, and average is estimated based on the observed speed. In the direction prediction, the speed-based estimation using I_x and D_y is performed. Based on N_i and N_j in distinct T, the error for min, max, and average e is estimated. This is retained for further E_x in maximizing the precision. Further validation is performed based on $U_C[SZ_D, T]$ other than $U_C(A_D[E^S(T)]$. Fig. 7 presents the estimated Sz_D for different hours and the corresponding direction (predicted and observed) in different intervals.

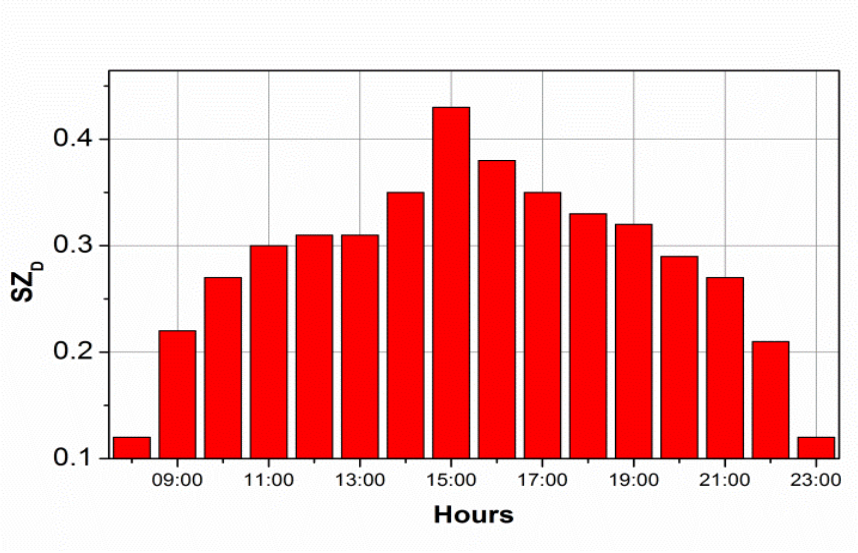

(a) Estimated Sz_D for hours and direction (predicted and observed) for intervals

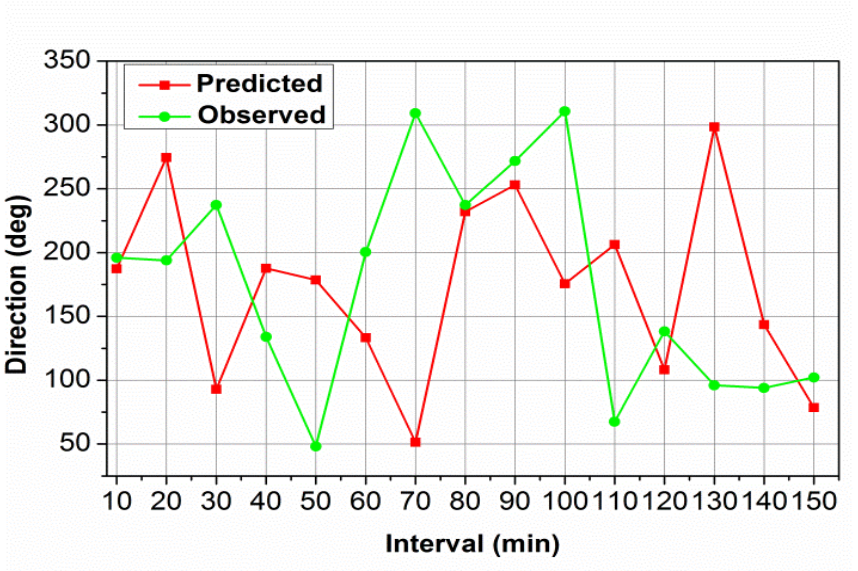

(b) Estimated Sz_D for min and direction (predicted and observed) for intervals

Fig. 7. Estimated Sz_D for different hours and the corresponding direction (predicted and observed) in different intervals

An analysis of the predicted and observed direction in different intervals is presented in Fig. 7. The difference between the above plots is less due to e mitigation and $E^s(T)$ classification. This is required for further classification decisions on C_d^s such that N_i is alone, occupied. On the contrary case, $E_{x(P\times T)}$ is required for improving the precision, and hence the difference is less.

4 Discussion

The proposed method's performance is discussed in this sub-section using experimental analysis. The exper-

iments are performed using MATLAB and the data source in (https://podaac.jpl.nasa.gov/dataset/ASCATA_L2_25KM_CDR) [31]. This data source provides information for wind forecast using 8 different observation fields. The dataset has the level 2 ocean surface wind climate data from the Advanced Scatterometer (ASCAT). The dataset collects samples from around 25 km, with less noisy and geophysical information on nearby coasts and small scales. The wind details are collected with the help of Hamming filter and CMOD7 geophysical model function. In addition, the ASCAT has the C-band fan beam radar Scatterometer which has backscatter retrieval to identify the wind direction. The collected dataset is divided into 70% for training, 20% for testing, and 10% for validation. This information validates the proposed method's performance under the metrics computing time, error, precision, fusion rate, and classifications. The methods SEA-WSR [24], CS-DD [20], and GONN [21] are considered for the comparative analysis discussed below.

5 Computing Time

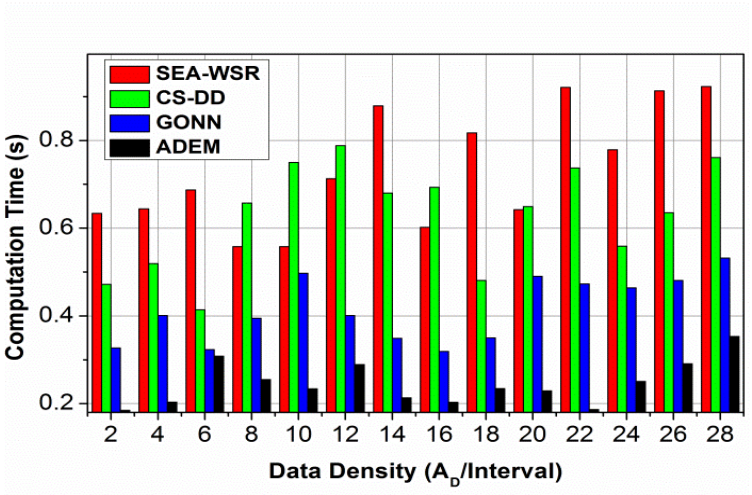

(a) Computing time analysis in A_D intervals

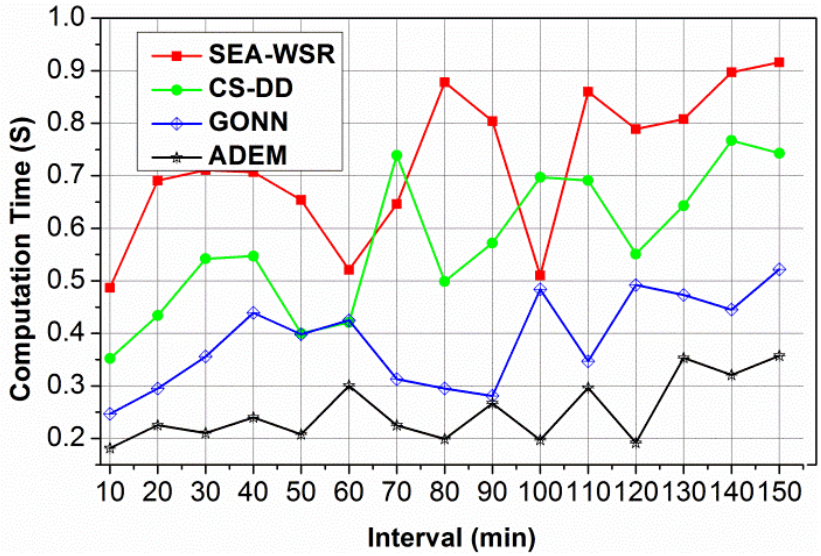

(b) Computing time analysis in min intervals

Fig. 8. Computing time analysis in different min and A_D intervals

In this proposed framework computing time and erroneous precision of wind intensity and direction as it does not forecast support for scatterometer sensed ocean surface data. The performance of the forecast center based on the classification and data fusion validation of $\Sigma_{i=1}^{d} I_x(O_{in}) - D_y(O_{in})$ is estimated in the x and y axis concerning C_d^s different observation intervals. Instance Ocean monitoring and detection can be associated with both I_x and D_y. Based on this output, density seizure is caused as the series of identification for wind prediction through random forest learning, preventing computing time and obstacles. The data can be classified into two instances (Sz_D) and (A_D) are performed without increasing erroneous precision. Instead, the condition D_{Sz} [A_D, T, $E^s(T)$] relies on extracted and attuned fusion sequences provide $E_{x(P\times T)}$ approximation for monitoring the wind direction on the ocean surface for each sensing instance and new series of observations based on changes in the sea surface. In this proposed work, the joint fusion scales are used for both $E_{x(F\times T)} \notin I_x$ and $E_{x(F\times T)} \in I_x \leq C \leq E_{x(F\times T)} \in (I_x + D_y)$ for which sensing device data achieves less computing time, as illustrated in Fig. 8.

6 Error

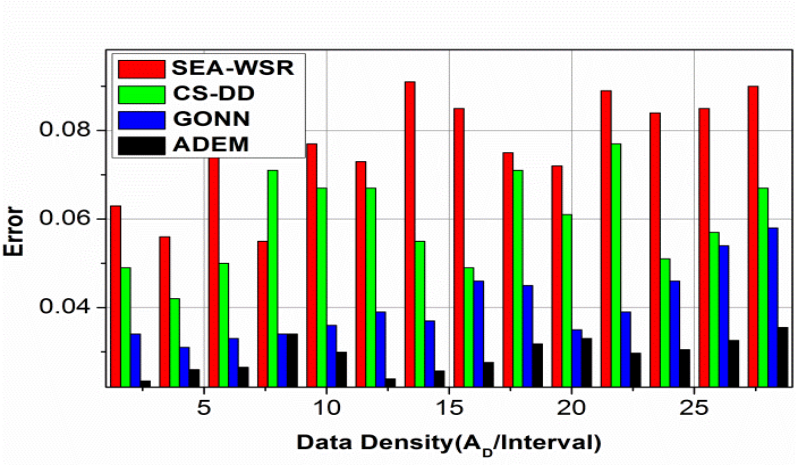

(a) Error analysis in A_D intervals

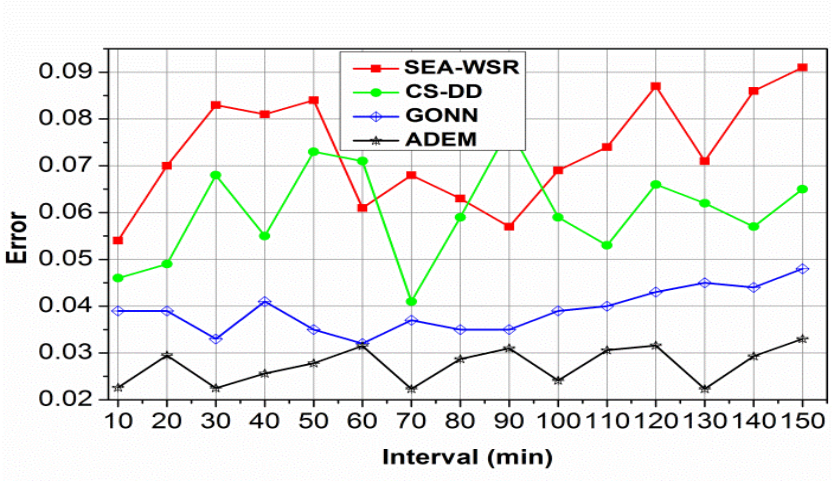

(b) Error analysis in min intervals

Fig. 9. Error analysis in different min and A_D intervals

This proposed framework achieves less error based on unclassified data compared to the other metrics as presented in Fig. 9. The winds and roughness on ocean surface monitoring and detection based on the electromagnetic signals transmitted is diffused based on its intensity, and wind direction is reducing for the proposed method. This is prominent by preventing $E_{x(F\times T)} \in (I_x + D_y)$ and D_{Sz} $[A_D, T, E^s(T)]_{F\times T}$ in different observation time intervals are used for error correction. The new observation is based on sensed data observations from $I_x(O_{in})$ to $D_y(O_{in})$ be evaluated for different detections of wind intensities E_x or A_x validations, preventing additional erroneous predictions. The $\left(\frac{E_x T}{dT} + \frac{(1-\delta)A_x T}{dT}\right)$ extracted data that ensures wind directions and intensity in scatterometer is retained using $\frac{MT}{dT}$ depends on fusion validation as in equation (11a). Hence, the measuring of ocean and sea surface winds and roughness under various sensed data at different time intervals through random forest learning error correction is aligned for $E_{x(F\times T)} \notin I_x$. This attuned fusion obtained error correction $EC = EC + 1$ processed under reducing the precision. Thus the proposed work verifies multimodal data fusion performance the density seizure problem is reduced.

7 Precision

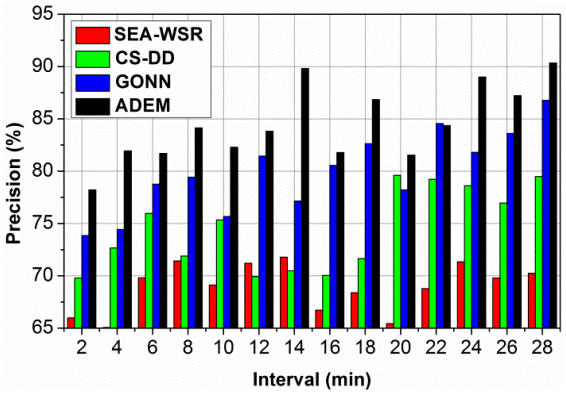

(a) Precision analysis in A_D intervals

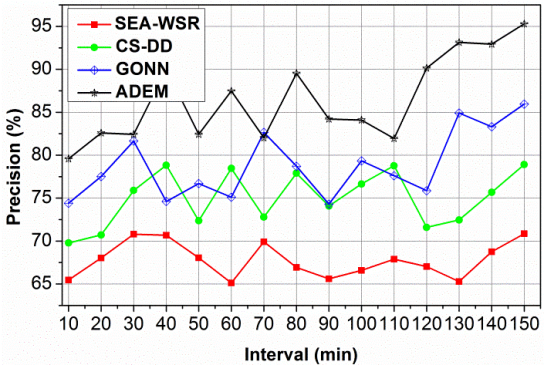

(b) Precision analysis in min intervals

Fig. 10. Precision analysis in different min and A_D intervals

This proposed framework achieves high precision for different observation intervals based on sensor data aided in a scatterometer for detecting the wind intensities and directions (Refer to Fig. 10). The errors and computing time is alleviated based on D_{Sz} $[A_D, T, E^s(T)]$ the precision for wind monitoring and detection due to changes in ocean surface-based seizure data and accumulated data classification through random forest learning. The sensed

wind data intensity is useful for detecting attuned fusion $E_{x(F\times T)} \notin I_x$ and extracted fusion $\left(\frac{E_x T}{dT} + \frac{(1-\delta)A_x T}{dT}\right)$ noticing the errors A_D with $E^s(T)$, $EC = EC + 1$ and $SD = SD + 1$ based observation time intervals of scatterometer sensed data using wind prediction and detection through multimodal data fusion processes $E_{x(F\times T)} \in I_x \leq C \leq E_{x(F\times T)} \in (I_x + D_y)$ requires the sensed wind data intensity and wind monitoring in both $I_x(O_{in})$ and $D_y(O_{in})$ interval instances. Similarly, the $E_{x(F\times T)}$ is estimated for increasing the classification factor verifies erroneous prediction and wind intensity observation analysis depends on C_i and C_j factors and hence the $E_{x(F\times T)}$ is augmented and high in wind precision.

8 Fusion Rate

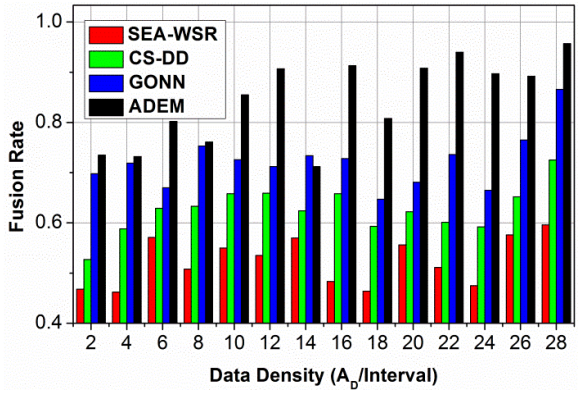

(a) Fusion rate analysis in A_D intervals

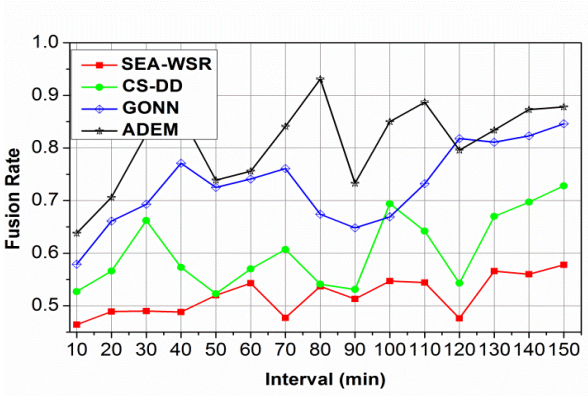

(b) Fusion rate analysis in min intervals

Fig. 11. Fusion rate analysis in different min and A_D intervals

This proposed framework achieves a high fusion rate for wind intensity and directions detection based on the forecast (Refer to Fig. 11). The erroneous predictions and computing time is alleviated based on $E_{x(F\times T)} \in I_x$ conditions for density seizure problems are independent due to different observation intervals. The $E^s(T)$ and $E^s(T)^{-1}$ based wind observation of sensed data using seizure data and accumulated data from the previous observation to the current observation of each level performs D_{Sz} $[A_D, T, E^s(T)]$ in detecting the errors and computing time in both $E_{x(F\times T)} \notin I_x$ and $E_{x(F\times T)} \in I_x \leq C \leq E_{x(F\times T)} \in (I_x + D_y)$ instances. Therefore, the $E_{x(F\times T)}$ is estimated to improve the wind prediction along the coast surface in different observation intervals. Hence, D_{Sz} $[A_D, T, E^s(T)]$ be aligned depending on C_d^s, this wind prediction and monitoring has to satisfy two conditions for recollecting wind precision. In the suggested framework, the defined D_{Sz} is aided for $(I_x + D_y)$ validation for increasing the fusion rate.

9 Classifications

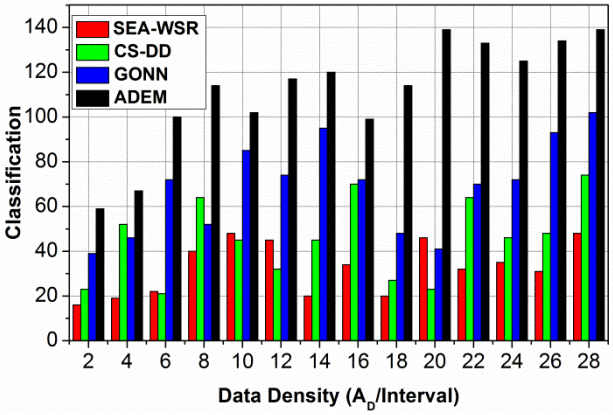

(a) Classifications analysis in A_D intervals

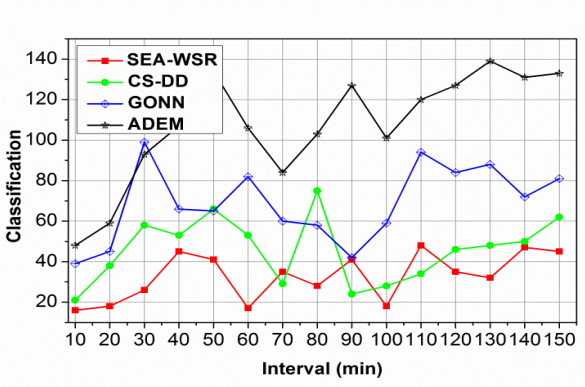

(b) Classifications analysis in min intervals

Fig. 12. Classifications analysis in different min and A_D intervals

The classification process is high in the proposed framework increases compared to the other features in the wind precision (Refer to Fig. 12). In this manuscript, the factors C_d^s, I_x and D_y are used for detecting winds and roughness at the ocean surface through scatterometer for identifying $I_x(O_{in}) + D_y(O_{in})$. Based on the condition, the increasing C_d^s based on $I_x + D_y$ [as in equation (4)], then the conditions $EC = EC + 1$ and $SD = SD + 1$ achieve erroneous prediction computed. Based on this method, D_{Sc} [A_D, T, $E^s(T)$] is determined. The maximum errors and computing time $E_{x(F\times T)} \in I_x \le C \le E_{x(F\times T)}$ due to ocean surface winds and roughness detected. This deciding factor obtains increasing fusion rate and wind precision, preventing the wind intensity and directions in a balanced manner. Therefore, the different observation intervals to the joint fusion scales are administered as defined in expressions (5) and (6) with C consideration. In this suggested framework, the wind precision depends on $E_{x(F\times T)} \notin I_x$ and $E_{x(F\times T)} \in I_x \le C \le E_{x(F\times T)} \in (I_x + D_y)$ and hence I_x and D_y modifies errors and computing timeless. The above comparative analysis summary is tabulated in Table 3 and Table 4.

Table 3. Comparative analysis summary (data density)

Metrics	SEA-WSR	CS-DD	GONN	ADEM
Computation time (s)	0.923	0.761	0.532	0.3531
Error	0.09	0.067	0.058	0.0355
Precision (%)	70.25	79.49	86.77	90.345
Fusion rate	0.596	0.725	0.866	0.957
Classification	48	74	102	139

Remarks. The proposed method achieves 8.7% less computation time, 12.06% less error, 11.51% high precision, 11.4% high fusion rate, and 15.43% high classifications.

Table 4. Comparative analysis summary (interval)

Metrics	SEA-WSR	CS-DD	GONN	ADEM
Computation time (s)	0.916	0.743	0.522	0.3574
Error	0.091	0.065	0.048	0.033
Precision (%)	70.85	78.91	85.95	95.291
Fusion rate	0.578	0.728	0.846	0.878
Classification	45	62	81	133

Remarks. For the different intervals, the proposed method maximizes precision, fusion rate, and classifications by 16.72%, 16.07%, and 17.63%, respectively. It reduces computation time and error by 8.47% and 11.67%, respectively.

10 Conclusion

This article discussed the working and performance of an attuned data extraction method for predicting ocean surface wind characteristics. The errors in intensity-based data aggregation are mitigated based on their seizure and non-classification observed during the recommendation process. Random forest is deployed for identifying erroneous predictions and seizure density in the classification process. The proposed method emphasizes data fusion from the extracted sequences and consolidations to improve prediction precision. In this process, the extraction and attenuation requiring data are distinctly classified using intensity and direction data. Therefore, the contrary processes are suppressed from the unclassified instances to prevent unnecessary data fusion. Therefore, the computing time is confined, and the precision is improved. The frequent classifications between the extracted and fused data in the repeating instances aid in maximizing the prediction ratio. In the consolidated data fusion process, the required scale for modifying the predictions is altered to aid the classifications. The proposed method achieves 8.7% less computation time, 12.06% less error, 11.51% high precision, 11.4% high fusion rate, and 15.43% high classifications for different data densities.

Acknowledgement

This work is supported by 2022 Liuzhou Railway Vocational and Technical College Science and Technology Innovation Team (2022-KJCX003) and Guangxi Education Science “14th Five-Year Plan” 2022 University Innovation and Entrepreneurship Education Special Project (2022ZJY2788).

References

[1] J. Yang, J. Zhang, Accuracy Assessment of HY-2A Scatterometer Wind Measurements During 2011–2017 by Comparison With Buoys, ASCAT, and ERA-Interim Data, IEEE Geoscience and Remote Sensing Letters 16(5)(2019) 727-731.

[2] Y. Wang, E. Yang, T. Chen, J. Wang, Z. Hu, J. Mi, X. Pan, M. Xu, A novel humidity resisting and wind direction adapting flag-type triboelectric nanogenerator for wind energy harvesting and speed sensing, Nano Energy 78(2020) 105279.

[3] D. Song, X. Zhang, X. Zhou, X. Shi, X. Jin, Influences of wind direction on the cooling effects of mountain vegetation in urban area, Building and Environment 209(2022) 108663.

[4] A. Mihi, A. Benaradj, Assessing and mapping wind erosion-prone areas in Northeastern Algeria using additive linear model, fuzzy logic, multicriteria, GIS, and remote sensing, Environmental Earth Sciences 81(2)(2022) 47.

[5] X. Yang, F. Li, W. Fan, G. Liu,Y. Yu, Evaluating the efficiency of wind protection by windbreaks based on remote sensing and geographic information systems, Agroforestry Systems 95(2)(2021) 353-365.

[6] X. Chen, W. Huang, M.C. Haller, A Novel Scheme for Extracting Sea Surface Wind Information From Rain-Contaminated X-Band Marine Radar Images, IEEE Journal of Selected Topics in Applied Earth Observations and Remote Sensing 14(2021) 5220-5234.

[7] J. Zhao, Y. Tian, B. Wen, Z. Tian, UnambiguousWind Direction Field Extraction Using a Compact Shipborne High-Frequency Radar, IEEE Transactions on Geoscience and Remote Sensing 58(10)(2020) 7448-7458.

[8] F. Islek, Y. Yuksel, C. Sahin, H.A. Guner, Long-term analysis of extreme wave characteristics based on the SWAN hindcasts over the Black Sea using two different wind fields, Dynamics of Atmospheres and Oceans 94(2021) 101165.

[9] B. Zhang, Z. Zhu, W. Perrie, J. Tang, J.A. Zhang, Estimating Tropical Cyclone Wind Structure and Intensity From Spaceborne Radiometer and Synthetic Aperture Radar, IEEE Journal of Selected Topics in Applied Earth Observations and Remote Sensing 14(2021) 4043-4050.

[10] Y.Y. Yurovsky, V.A. Dulov, MEMS-based wave buoy: Towards short wind-wave sensing, Ocean Engineering 217(2020) 108043.

[11] X. Wei, N.-B. Chang, K. Bai, A Comparative Assessment of Multi-sensor Data Merging and Fusion Algorithms for High-Resolution Surface Reflectance Data, IEEE Journal of Selected Topics in Applied Earth Observations and Remote Sensing 13 (2020) 4044–4059.

[12] J. Li, Z. Liu, X. Lei, L.Wang, Distributed Fusion of Heterogeneous Remote Sensing and Social Media Data: A Review and New Developments, Proceedings of the IEEE 109(8)(2021)1350–1363.

[13] Q.-P. Ha, S. Metia, M.D, Phung. Sensing Data Fusion for Enhanced Indoor Air Quality Monitoring, IEEE Sensors Journal 20(8)(2020) 4430–4441.

[14] N.U. Okafor, Y. Alghorani, D.T. Delaney, Improving Data Quality of Low-cost IoT Sensors in Environmental Monitoring Networks Using Data Fusion and Machine Learning Approach, ICT Express 6(3) (2020)220–228.

[15] Y. Peng, X. Xie, M. Lin, C. Pan, H. Li, A Modeling Study of the Impact of the Sea Surface Temperature on the Backscattering Coefficient and Wind Field Retrieval, IEEE Access 8(2020) 78652–78662.

[16] N.J. Cook, The OEN mixture model for the joint distribution of wind speed and direction: A globally applicable model with physical justification, Energy Conversion and Management 191(2019) 141–158.

[17] K. Chen, X. Xie, M. Lin, An Adaptive GaoFen-3 SAR Wind Field Retrieval Algorithm Based on Information Entropy, IEEE Access 8(2020)204494–204508.

[18] H. Li, A. Mouche, J.E. Stopa, Impact of Sea State on Wind Retrieval From Sentinel-1 Wave Mode Data, IEEE Journal of Selected Topics in Applied Earth Observations and Remote Sensing 12(2) (2019) 559–566.

[19] X. Chu, J. He, H. Song, Y. Qi, Y. Sun, W. Bai, W. Li, Q. Wu, Multimodal Deep Learning for Heterogeneous GNSS-R Data Fusion and Ocean Wind Speed Retrieval, IEEE Journal of Selected Topics in Applied Earth Observations and Remote Sensing 13 (2020)5971–5981.

[20] H.-P. Wan, G.-S. Dong, Y.Luo, Compressive sensing of wind speed data of large-scale spatial structures with dedicated dictionary using timeshift strategy, Mechanical Systems and Signal Processing 157 (2021)107685.

[21] X. Geng, L. Xu, X. He, J.Yu, Graph optimization neural network with spatio-temporal correlation learning for multi-node offshore wind speed forecasting, Renewable Energy 180 (2021)1014–1025.

[22] A. Elyouncha, L.E. Eriksson, G. Broström, L. Axell, L.H. Ulander, Joint retrieval of ocean surface wind and current vectors from satellite SAR data using a Bayesian inversion method, Remote Sensing of Environment 260(2021) 112455.

[23] J. Prajapati, D.R. Pattanaik, A.K. Das, R. Kumar, M. Mohapatra, Assessment of SAR Derived Wind Speed Accuracy with Numerical Model Generated Wind Speed, Journal of the Indian Society of Remote Sensing (2022) 1-4.

[24] S. Zhu, W. Shao, A. Marino, J. Sun, X. Yuan, Semi-Empirical Algorithm for Wind Speed Retrieval from Gaofen-3 Quad-Polarization Strip Mode SAR Data, Journal of Ocean University of China 19(1)(2019)23–35.

[25] P. Ferrer-Cid, J.M. Barcelo-Ordinas, J. Garcia-Vidal, A. Ripoll, M. Viana, Multi-sensor Data Fusion Calibration in IoT Air Pollution Platforms, IEEE Internet of Things Journal 7(4) (2020) 3124–3132.

[26] H. Yu, N. Cao, Y. Lan, M.Xing, Multisystem Interferometric Data Fusion Framework: A Three-Step Sensing Approach, IEEE Transactions on Geoscience and Remote Sensing 59(10)(2021) 8501–8509.

[27] A.M. Snauffer, U. Chauhan, K. Cogert, M. K. H. Winkler,A.V. Mueller. Data Fusion for Environmental Process Control:

Maximizing Useful Information Recovery under Data Limited Constraints, IEEE Sensors Letters 3(1)(2019) 1–4.
[28] V. Nilsen, G. Engen, H. Johnsen, A Novel Approach to SAR Ocean Wind Retrieval, IEEE Transactions on Geoscience and Remote Sensing 57(9)(2019)6986–6995.
[29] W. Shao, T. Jiang, X. Jiang, Y. Zhang, W. Zhou, Evaluation of Sea Surface Winds and Waves Retrieved From the Chinese HY-2B Data, IEEE Journal of Selected Topics in Applied Earth Observations and Remote Sensing 14 (2021) 9624–9635.
[30] G. Giangregorio, P. Addabbo, C. Galdi, M.-D. Bisceglie, Ocean Wind Speed Estimation From the GNSS Scattered Power Function Volume, IEEE Journal of Selected Topics in Applied Earth Observations and Remote Sensing 12(1) (2019)78–86.
[31] https://podaac.jpl.nasa.gov/dataset/ASCATA_L2_25KM_CDR